Fiber-Directed Conjugated-Polymer Torsional Actuator: Nonlinear Elasticity Modeling and Experimental Validation

Yang Fang, *Member, IEEE*, Thomas J. Pence, and Xiaobo Tan, *Member, IEEE*

***Abstract*—Existing conjugated-polymer actuators typically take the form of benders or linear extenders. In this paper, a conjugated-polymer-based torsional actuator is proposed by embedding helically wound fibers into a conjugated polymer tube during the polymer-deposition process. Upon actuation, the electrolyte-soaked tube swells, and consequently, produces torsion and other associated deformations because of fiber-induced mechanical anisotropy of the composite material. A nonlinear elasticity-based model is presented to capture the torsion, elongation, and dilation of the tube. Experiments on tubular actuators with different thicknesses, fiber-winding angles, and diameters confirm the aforementioned deformation modes and validate the effectiveness of the proposed model.**

***Index Terms*—Actuators, conjugated polymer, electroactive polymers, nonlinear elasticity, modeling.**

I. Introduction

CONJUGATED polymers, also called conducting polymers, have intrinsic actuation [1], [2] and sensing [3], [4] properties. These polymers have alternating single and double carbon–carbon bonds (conjugation). With an applied positive potential, electrons can be removed from the polymer chains (oxidation). If the polymer is in contact with an electrolyte, the positively charged polymer backbone will attract negatively charged ions (anions) into the polymer matrix and/or repel positively charged ions (cations) out of the matrix. The effect can be reversed when a negative potential is applied to the polymer (reduction). Transport of the ions in and out of the polymer matrix during reduction–oxidation (redox) induces volumetric change, namely swelling or deswelling, which is believed to be the primary actuation mechanism for conjugated polymers [2].

Manuscript received November 13, 2009; revised March 4, 2010; accepted April 16, 2010. Date of publication June 3, 2010; date of current version May 11, 2011. Recommended by Technical Editor Y. Sun. The work of Y. Fang and X. Tan was supported in part by National Science Foundation CAREER Grant ECCS 0547131 and in part by the Michigan State University Intramural Research Grants Program under Grant 05-IRGP-418. The work of T. Pence was supported by National Science Foundation Grant CMMI 0510600.

Y. Fang is with the Engine, Emissions, and Vehicle Research Division, Southwest Research Institute, Ann Arbor, MI 48105 USA (e-mail: fangyang@msu.edu).

T. J. Pence is with the Department of Mechanical Engineering, Michigan State University, East Lansing, MI 48824 USA (e-mail: pence@egr.msu.edu).

X. Tan is with the Smart Microsystems Laboratory, Department of Electrical and Computer Engineering, Michigan State University, East Lansing, MI 48824 USA (e-mail: xbtan@egr.msu.edu).

Color versions of one or more of the figures in this paper are available online at http://ieeexplore.ieee.org.

Digital Object Identifier 10.1109/TMECH.2010.2049366

Reported conjugated-polymer actuators have typically been used as linear extenders or benders. The dimensional changes of a single piece of conjugated polymer during redox can directly be exploited to produce linear motion [5], [6]. On the other hand, a conjugated-polymer layer bonded to a nonswelling layer [2] or another conjugated-polymer layer, but with different swelling [7]–[10], results in bending motion. These configurations have been explored in various biomedical [2], biological [11], microfluidic [12], [13], and robotic [14], [15] applications. In many applications, however, more sophisticated deformation modes will be highly desirable. Torsion, for example, can greatly enhance the dexterity of microsurgical tools.

In this paper, a novel, conjugated-polymer-based torsional actuator is proposed by embedding helically wound fibers into a conjugated-polymer tube. The concept is motivated by the fact that fiber-reinforced elastic materials can generate complicated deformation when the materials swell/deswell [16]–[18]. As the fibers have little room for extension, they impose directional constraints for swelling of the material matrix, which results in sophisticated deformation determined by the fiber-matrix arrangement. For example, theoretical investigation has predicted torsion and other deformation modes for a swelling hyperelastic tube with helical fiber reinforcement [19]. Biology provides interesting insight as well. Directionally modulated swelling and deswelling is the basis for the majority of controllable and repeatable motions in plants, including, e.g., vine twinning, petal opening, and leaf rolling [20]. Such directional modulation is typically achieved with preferential alignment of fibrils in the cell wall [21], [22].

We fabricate proof-of-concept prototypes for the proposed torsional actuators by helically embedding platinum fibers into a polypyrrole (PPy) tube during the PPy deposition. Electrically induced swelling/deswelling of PPy is then expected to result in torsion. Our fabrication process follows the work of Ding *et al.* [23]. Note that the adoption of tubular geometry and helical wires in [23] was for a completely different purpose—increasing the electrical conductivity of the actuator, and torsional motion was not investigated in that work.

A nonlinear elasticity model is then presented to capture the swelling-induced large deformation for the fiber-directed, conjugated-polymer tubular actuator. The strains generated by PPy actuators are typically between 1% and 10% [5], [24], and a 20% contraction has been observed in the thickness direction of a polyaniline (PANI) film [25]. Therefore, linear elasticity theory based on small strains is often inadequate for describing the large deformation in conjugated-polymer actuators. Our

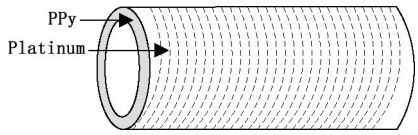

Fig. 1. Schematic of the conjugated-polymer-based torsional actuator.

earlier work has shown the superiority of nonlinear elasticity modeling over linear elasticity modeling for trilayer PPy benders [26]. Another advantage of a nonlinear model is its generality for incorporating sophisticated interactions. In this paper, the elastic energy under actuation-induced swelling captures both the strain energy of the PPy matrix and the strain energy of embedded fibers. Nonlinear material behaviors can be incorporated through the specification of strain energy functions. With the enforcement of proper boundary conditions, force and moment balance equations are formulated and solved to obtain the actuation-induced deformation.

Tubular, fiber-directed PPy actuators with different thicknesses, fiber-winding angles, and diameters have been fabricated and tested. Experiments have not only confirmed torsion and associated elongation and radial dilation, as predicted by the nonlinear model, but also validated the models quantitatively for different actuator dimensions and fiber pitch angles. Therefore, we have established the utility of the model for actuator design and optimization.

The remainder of this paper is organized as follows. The fabrication process of the actuator is described in Section II. The nonlinear mechanics modeling framework is described in Section III. Experimental validation of the nonlinear model is presented Section IV. Finally, concluding remarks are provided in Section V.

II. Actuator Fabrication

As illustrated in Fig. 1, the proposed actuator consists of a PPy tube with platinum fibers helically wound around the tube. It is critical to achieve integrative embedding of the fibers within the polymer matrix, so that the fibers will deform with the polymer matrix instead of cutting through the matrix during swelling/deswelling of the polymer. As described next, this can be realized by depositing PPy onto a tubular substrate, around which the platinum wire is wound.

A glass cylinder is used as the substrate. It is coated uniformly with gold through sputtering. A platinum wire with diameter of 25 μm is wound uniformly along the glass cylinder at a fixed pitch angle. The tube is then soaked in a mixture of 0.1 M pyrrole, and 0.1 M $\mathrm{Li}^{+}\mathrm{TFSI}^{-}$ in propylene carbonate (PC) with 0.5% (by weight) water [7], and connected to the working electrode of a potentiostat (OMNI101 from Cypress Systems). To maintain a constant potential on the PPy when the PPy grows on the surface of the glass tube, an Ag/AgCl reference electrode (Aldrich Chemical) is used. A stainless-steel mesh with large surface area serves as the auxiliary electrode. The auxiliary electrode, also known as the counter electrode, has a potential opposite in sign to that of the working electrode, and it is where the byproducts of the electrochemical process deposit [27]. The large surface area of the auxiliary electrode ensures that little current goes through the reference electrode, which is important for maintaining the potential of the latter electrode. The fabrication setup is illustrated in Fig. 2. The electric current density is maintained at 2 $\mathrm{mA/cm^2}$. The thickness of PPy grown on the glass substrate is controlled through the deposition time. Because the PPy layer has poor adhesion to the underlying gold layer, it can be easily taken off from the glass cylinder. Fig. 3 shows a fabricated prototype of the fiber-directed PPy tube, where the inner and outer diameters are 2.5 and 3 mm, respectively.

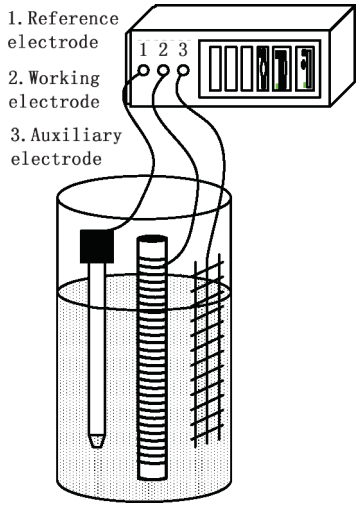

Fig. 2. Experimental setup for fabricating the fiber-directed conjugated-polymer actuator.

Fig. 3. Fabricated platinum fiber-directed PPy tube.

III. Nonlinear Elasticity Modeling of the Torsional Actuator

When a positive voltage is applied between the fiber-directed PPy tube and an electrolyte, anions in the electrolyte will move toward and accumulate at the PPy/electrolyte interface, thus forming a double layer of charges (see Fig. 4). The highly concentrated ions in the double layer will diffuse into the PPy. When a negative voltage is applied, the PPy is reduced and the previously absorbed ions will be repelled back to the electrolyte. Mass transport of ions in and out of the polymer causes swelling and deswelling of the tube, which subsequently leads to deformation because of mechanical interaction between the PPy

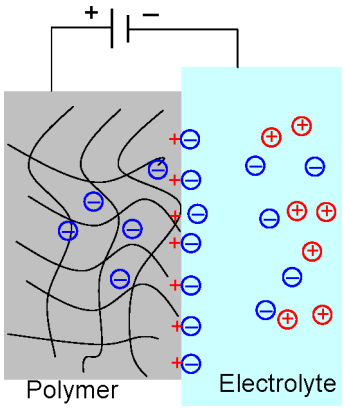

Fig. 4. Illustration of double-layer charging and diffusion for a conjugated-polymer film in contact with an electrolyte.

matrix and the constraining fibers. The description of the actuation process can thus be roughly separated into three cascaded modules: an electrochemical module capturing the ion-transport dynamics [28]–[30], a swelling-to-charge coupling module, and a mechanical module capturing the swelling-induced deformation. For the proposed PPy tube actuator, the first two modules will be the same as for other configurations (e.g., trilayer benders [29]). Therefore, to highlight the third module, we will consider quasi-static voltage inputs, in which case the first module degenerates to a proportional constant relating the net charge density ρ to the applied voltage U. This is briefly explained next before we elaborate on the nonlinear mechanics framework.

Under a quasi-static voltage U, the total transferred charges Q can be calculated as follows [29]:

$$Q = -k_1 U. \tag{1}$$

In (1), k_1 is determined via $k_1 = (1/2)(1 + (h/\delta))C$, where h is the thickness of the PPy layer, δ is the thickness of the double-layer at the polymer/electrolyte interface, and C represents the double-layer capacitance [29]. The proportionality constant k_1 can be obtained on an experimental basis. The transferred charge density ρ is given by

$$\rho = \frac{Q}{V} \tag{2}$$

where V is the volume of the PPy layer. The volumetric change in the PPy induced by the ion transport can be captured by [31]:

$$\nu = \frac{V - k_2 \rho V}{V} = 1 - k_2 \rho \tag{3}$$

where ν represents the swelling ratio of the PPy layer and k_2 is the swelling-to-charge ratio. When $\nu > 1$, the volume is increased; when $\nu < 1$, the volume is decreased. The value of k_2 has the order of 10^{-10} $\mathrm{m}^3/\mathrm{Coulomb}$ [28].

Given the swelling ratio ν, we next discuss how to model the resulting deformation with a nonlinear mechanics framework.

A. Nonlinear Mechanical Modeling Framework

The original and deformed configurations are shown in Fig. 5, where $\mathbf{F}$ represents the deformation gradient, which can map

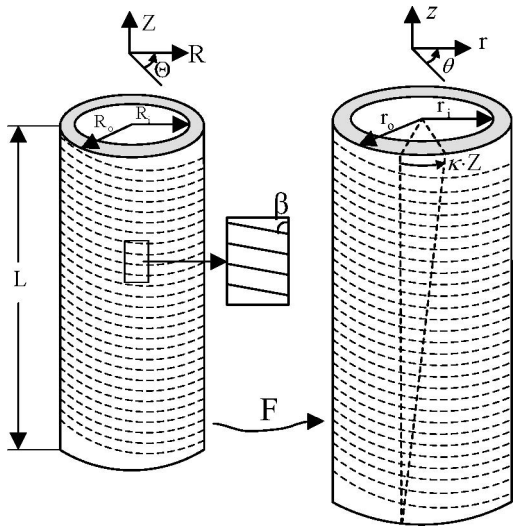

Fig. 5. Illustration of the actuator configuration. (Left) Original configuration. (Right) Deformed configuration.

vectors (expressed with a Z, R, Θ domain) in the original configuration to vectors (expressed with a z, r, θ domain) in the deformed configuration. The pitch angle β ($0° < \beta < 90°$) [19], as defined graphically in Fig. 5, specifies the fiber-winding direction.

The deformation can be characterized by the following equations:

$$r = r(R) \qquad \theta = \Theta + \kappa Z \qquad z = \lambda_z Z \tag{4}$$

where κ is the twist per unit length and λ_z is the elongation per unit length in the longitudinal direction. Suppose that the deformation takes a particle at location $\mathbf{X}$ in the reference configuration to the location $\mathbf{x}$ in the deformed configuration. The deformation gradient is defined as follows:

$$\mathbf{F} = \frac{\partial \mathbf{x}}{\partial \mathbf{X}} \tag{5}$$

or, $d\mathbf{x} = \mathbf{F} d\mathbf{X}$. For the polar coordinate system at hand

$$d\mathbf{X} = dR\mathbf{e}_R + Rd\Theta\mathbf{e}_\Theta + dZ\mathbf{e}_Z$$
$$d\mathbf{x} = dr\mathbf{e}_r + rd\theta\mathbf{e}_\theta + dz\mathbf{e}_z$$

where $\mathbf{e}_R, \mathbf{e}_\Theta$, and $\mathbf{e}_Z$ are the orthonormal unit vectors in the original configuration, and $\mathbf{e}_r, \mathbf{e}_\theta$, and $\mathbf{e}_z$ are the orthonormal unit vectors in the deformed configuration. The deformation gradient tensor is

$$\mathbf{F} = \frac{dr}{dR}\mathbf{e}_r \otimes \mathbf{e}_R + \frac{r}{R}\mathbf{e}_\theta \otimes \mathbf{e}_\Theta + \kappa r \mathbf{e}_\theta \otimes \mathbf{e}_Z + \lambda_z \mathbf{e}_z \otimes \mathbf{e}_Z \tag{6}$$

where $\otimes$ is the dyadic product. We assume that PPy is mechanically incompressible both before and after swelling. This assumption is based on relevant literature [32]. Therefore, the deformation satisfies the constraint that the volume is not changed by the motion after swelling, which means that the determinant of $\mathbf{F}$ satisfies

$$\det \mathbf{F} = \nu. \tag{7}$$

This, together with (6), implies

$$\frac{1}{R}\lambda_z r\frac{dr}{dR}=\nu. \tag{8}$$

Rewriting (8) as $rdr=(\nu/\lambda_z)RdR$ and integrating, we get

$$r^2=r_i^2+\frac{2}{\lambda_z}\int_{R_i}^{R}\nu RdR \tag{9}$$

where R_i and r_i are the inner radii of the tube in the original configuration and the deformed configuration, respectively. The left Cauchy–Green deformation tensor is defined by

$$\mathbf{B}=\mathbf{F}\mathbf{F}^{\mathbf{T}}. \tag{10}$$

Following (6) and (8), $\mathbf{B}$ can be further expressed as follows:

$$\mathbf{B}=\frac{\nu^2R^2}{\lambda_z^2r^2}\mathbf{e}_r\otimes\mathbf{e}_r+\left(\kappa^2+\frac{1}{R^2}\right)r^2\mathbf{e}_\theta\otimes\mathbf{e}_\theta +\kappa\lambda_z r(\mathbf{e}_\theta\otimes\mathbf{e}_z+\mathbf{e}_z\otimes\mathbf{e}_\theta)+\lambda_z^2\mathbf{e}_z\otimes\mathbf{e}_z. \tag{11}$$

The principal invariants of $\mathbf{B}$ are defined as follows:

$$I_1=\mathrm{tr}(\mathbf{B})\qquad I_2=I_3\mathrm{tr}(\mathbf{B}^{-1})\qquad I_3=\det(\mathbf{B}) \tag{12}$$

where "tr" denotes the trace. From (11), the invariant I_1 is obtained as follows:

$$I_1=\frac{\nu^2R^2}{\lambda_z^2r^2}+\frac{r^2}{R^2}+\kappa^2r^2+\lambda_z^2. \tag{13}$$

The elastic energy function of PPy, denoted as Φ_m, can be modeled in the neo-Hookean form

$$\Phi_m=\frac{1}{2}\mu(I_1-3\nu^{2/3}) \tag{14}$$

where μ is an elasticity constant that can be taken as $E_{PPy}/3$, where $E_{PPy}=80$ MPa is the Young's modulus of PPy [26].

Let $\mathbf{M}$ be the unit vector in the reference configuration that defines the fiber direction in the material matrix

$$\mathbf{M}=\sin\beta\mathbf{e}_\Theta+\cos\beta\mathbf{e}_Z \tag{15}$$

where β is the pitch angle defined in Fig. 5. Given the deformation gradient $\mathbf{F}$, the unit vector $\mathbf{M}$ is mapped into

$$\mathbf{m}=\mathbf{F}\mathbf{M}=\left(\kappa\cos\beta+\frac{1}{R}\sin\beta\right)r\mathbf{e}_\theta+\lambda_z\cos\beta\mathbf{e}_z. \tag{16}$$

The fiber stretch ratio under actuation, denoted as λ_{fib}, is determined by

$$\lambda_{\mathrm{fib}}^2=\mathrm{tr}(\mathbf{m}\otimes\mathbf{m})=\left(\kappa\cos\beta+\frac{1}{R}\sin\beta\right)^2r^2+\lambda_z^2\cos^2\beta. \tag{17}$$

The strain energy function of the fiber can be modeled as follows:

$$\Phi_f=\frac{1}{2}\gamma(\lambda_{\mathrm{fib}}^2-1)^2 \tag{18}$$

where γ is a constant that captures the material stiffness in the fiber direction. In particular, it can be related to the effective Young's modulus of the material in the fiber direction by some proportionality factor [33]. The effective Young's modulus can be computed based on the Young's moduli of both the fiber and the material matrix, and on the cross-sectional area fraction of the fiber. For fibers that are much stiffer than the matrix, one may approximate γ as one quarter of the Young's modulus of the fiber phase times the fiber area fraction [33]. The area fraction depends on the specific way the fibers are embedded. For example, the tightest possible packing within a perfect cylindrical tube gives an area fraction of $\pi/2\sqrt{3}=0.907$. However, the fiber area fraction of our fabricated samples is difficult to determine, since their outer surfaces are grooved. In particular, the platinum fiber, located close to the inner wall of the tube, promotes the local growth of PPy during the electrochemical deposition process, thus resulting in a PPy tube with helical threads on the outer surface that are approximately 0.5 mm wide (see Fig. 3). An approximation of 0.8 is taken for the fiber area fraction in our subsequent calculations. Using 168 GPa for the value of the Young's modulus of platinum [34], we obtain $\gamma=34$ GPa.

Therefore, the total elastic energy of the fiber-directed PPy actuator is

$$W=\Phi_m+\Phi_f. \tag{19}$$

The Cauchy stress tensor can be written as follows [19]:

$$\sigma=\frac{1}{\nu}\frac{\partial W}{\partial\mathbf{F}}\mathbf{F}^T-p\mathbf{I} \tag{20}$$

where p has the interpretation of the (unknown) hydrostatic pressure arising from (7), and $\mathbf{I}$ denotes the identity tensor. With the expression of elastic energy in (19), the Cauchy stress is [19]

$$\sigma=\frac{2}{\nu}\frac{\partial\Phi_m}{\partial I_1}\mathbf{B}+\frac{1}{\nu\lambda_{\mathrm{fib}}}\frac{\partial\Phi_f}{\partial\lambda_{\mathrm{fib}}}\mathbf{m}\otimes\mathbf{m}-p\mathbf{I}. \tag{21}$$

Considering (11) and (16), we can express (21) as follows:

$$\sigma=\sigma_{rr}\mathbf{e}_r\otimes\mathbf{e}_r+\sigma_{\theta\theta}\mathbf{e}_\theta\otimes\mathbf{e}_\theta +\sigma_{\theta z}(\mathbf{e}_\theta\otimes\mathbf{e}_z+\mathbf{e}_z\otimes\mathbf{e}_\theta)+\sigma_{zz}\mathbf{e}_z\otimes\mathbf{e}_z \tag{22}$$

where

$$\sigma_{rr}=-p+\frac{\mu\nu R^2}{\lambda_z^2r^2} \tag{23}$$

$$\sigma_{\theta\theta}=-p+\frac{\mu r^2}{\nu}\left(\kappa^2+\frac{1}{R^2}\right)+\frac{2\gamma r^2}{\nu}\left(\kappa\cos\beta+\frac{1}{R}\sin\beta\right)^2(\lambda_{\mathrm{fib}}^2-1) \tag{24}$$

$$\sigma_{zz}=-p+\frac{\mu}{\nu}\lambda_z^2+\frac{2\gamma}{\nu}\lambda_z^2(\lambda_{\mathrm{fib}}^2-1)\cos^2\beta \tag{25}$$

$$\sigma_{\theta z}=\frac{\mu}{\nu}\kappa\lambda_z r+\frac{2\gamma}{\nu}\lambda_z r\cos\beta\left(\kappa\cos\beta+\frac{1}{R}\sin\beta\right)(\lambda_{\mathrm{fib}}^2-1). \tag{26}$$

This framework is based upon strain energy functions and general deformation gradients, and it is thus valid for both small and large deformations.

B. Boundary Conditions

The boundary conditions on the conjugated-polymer actuator are specified as follows:

$$\sigma_{rr}|_{R=R_i} = 0 \qquad \sigma_{rr}|_{R=R_0} = 0 \tag{27}$$

where R_i and R_o are the inner and outer radii of the tube in the reference configuration, respectively. Equation (27) represents that there is no normal loading applied to the inner and outer surfaces of the tube. Note that R is used in (27) since r is also a function of R. The equilibrium equation $\mathrm{div}\sigma = 0$ in the directions of r, z, and θ can be written as follows:

$$\frac{\partial \sigma_{rr}}{\partial r} + \frac{1}{r}\frac{\partial \sigma_{r\theta}}{\partial \theta} + \frac{\partial \sigma_{rz}}{\partial z} + \frac{1}{r}(\sigma_{rr} - \sigma_{\theta\theta}) = 0 \tag{28}$$

$$\frac{\partial \sigma_{rz}}{\partial r} + \frac{1}{r}\frac{\partial \sigma_{\theta z}}{\partial \theta} + \frac{\partial \sigma_{zz}}{\partial z} + \frac{\sigma_{rz}}{r} = 0 \tag{29}$$

$$\frac{\partial \sigma_{r\theta}}{\partial r} + \frac{1}{r}\frac{\partial \sigma_{\theta\theta}}{\partial \theta} + \frac{\partial \sigma_{z\theta}}{\partial z} + \frac{2\sigma_{r\theta}}{r} = 0 \tag{30}$$

where $\sigma_{r\theta} = 0$ and $\sigma_{rz} = 0$ in the current case. Considering (24)–(26), one can show that (29) and (30) reduce to $\partial p/\partial z = 0$ and $\partial p/\partial \theta = 0$, which means that p is a function of r only. Given $\sigma_{r\theta} = 0$ and $\sigma_{rz} = 0$, one can write (28) as follows by using (8):

$$\frac{d\sigma_{rr}}{dR} = -\frac{\nu R}{\lambda_z r^2}(\sigma_{rr} - \sigma_{\theta\theta}) \tag{31}$$

which can be further expanded by considering (23)

$$\frac{dp}{dR} = \frac{\nu R}{\lambda_z r^2}(\sigma_{rr} - \sigma_{\theta\theta}) + \frac{\mu\nu}{\lambda_z^2}\frac{d}{dR}\left(\frac{R^2}{r^2}\right). \tag{32}$$

Integrating (32) after substituting from the expressions (23) and (24), one can obtain the following form of p by using the boundary condition $\sigma_{rr}|_{R=R_0} = 0$:

$$p = \frac{\nu R^2 \mu}{\lambda_z^2 r^2} - \int_R^{R_o}\left(\mu\left(\frac{\nu^2 R^3}{\lambda_z^3 r^4} - \frac{R^2\kappa^2 + 1}{\lambda_z R}\right) - \frac{2R\gamma}{\lambda_z}\left(\kappa\cos\beta + \frac{1}{R}\sin\beta\right)^2(\lambda_{\mathrm{fib}}^2 - 1)\right)dR. \tag{33}$$

The other boundary condition $\sigma_{rr}|_{R=R_i} = 0$, with the aid of (23) and (33), gives the following equation:

$$\Delta = 0 \tag{34}$$

where

$$\Delta = \int_{R_i}^{R_o}\left(\frac{\mu}{2}\left(-\frac{\nu^2 R^2}{\lambda_z^2 r^4} + \kappa^2 + \frac{1}{R^2}\right) + \left(\kappa\cos\beta + \frac{1}{R}\sin\beta\right)^2\gamma(\lambda_{\mathrm{fib}}^2 - 1)\right)RdR. \tag{35}$$

C. Nonlinear Model

One can see from Fig. 5 that one function and two scalars quantify the deformed configuration: $r(R)$, λ_z, and κ. Because the profile of $r(R)$ can be calculated based on (9), variable r is determined by r_i. Hence, the deformation is completely characterized by the three scalars: r_i, λ_z, and κ. Equation (34) has provided one equation relating these scalars. The other two equations require knowledge of the applied moment T (about the tube axis) and the axial load Q, which are related to the stress by the following expressions:

$$T = 2\pi\int_{r_i}^{r_o}\sigma_{\theta z} r^2 dr \tag{36}$$

$$Q = 2\pi\int_{r_i}^{r_o}\sigma_{zz} r dr. \tag{37}$$

When one end of the tube is not constrained, it follows that $T = 0$ and $Q = 0$. These two equations, along with (34), provide three nonlinear equations for r_i, κ, and λ_z. One finds that the expression (35) is strongly dependent on r_i, the expression (36) for T is strongly dependent on κ, and the expression (37) for Q is strongly dependent on λ_z. In general, the numerical analysis to obtain these variables by solving three nonlinear equations is laborious. Therefore, in this paper, λ_z, representing the length change ratio in the axial direction, will be measured and used as a given parameter. Since Δ and T give the strongest dependence on r_i and κ, the equations $\Delta = 0$ and $T = 0$ are retained in the analysis and numerically solved to obtain r_i and κ.

By substituting from (26), one can integrate (36) and obtain the following expression:

$$T = \mu a\kappa + \gamma(b_0 + b_1\kappa + b_2\kappa^2 + b_3\kappa^3) \tag{38}$$

where a, b_0, b_1, b_2, and b_3 are terms involving λ_z, r_i, and the material constants. Similarly, one can integrate (35) and obtain an expression for Δ in the form

$$\Delta = \mu\Omega + \gamma\Gamma \tag{39}$$

where Ω and Γ are also terms involving material properties and λ_z, κ, and r_i. Detailed expressions for these terms are lengthy and will not be listed in this paper due to the space limitation. The two unknown variables r_i and κ can be obtained by numerically solving the coupled equations $\Delta = 0$ and $T = 0$ using (38) and (39).

IV. Experimental Results

A. Sample Preparation and Experimental Setup

Fiber-directed PPy tubular actuators were fabricated following the processes described in Section II. The tube has three important geometric parameters: its inner radius R_i, thickness $t = R_o - R_i$, and the fiber-winding pitch angle β. In order to study the influence of these parameters on actuation performance and to validate the scalability of the proposed nonlinear model, we fabricated four samples with different geometric configurations, as listed in Table I. In particular, Sample 1 and Sample 2 had the same tube thickness (0.381 mm) and pitch angle (80°), but different inner radii (2.2 mm versus 1.3 mm), where the variation of the inner radius was realized by using glass tube substrates with different diameters. Sample 3 had the same pitch angle and inner radius as Sample 1, but it had different thickness (0.686 mm). The thickness of a sample was controlled through the PPy deposition time. Finally, Sample 4 had the same thickness and inner radius as Sample 3, but it had

TABLE I
GEOMETRIC PARAMETERS OF FOUR SAMPLES USED IN EXPERIMENTS

	thickness (mm)	pitch angle (°)	radius (mm)
Sample 1	0.381	80	2.2
Sample 2	0.381	80	1.3
Sample 3	0.686	80	2.2
Sample 4	0.686	60	2.2

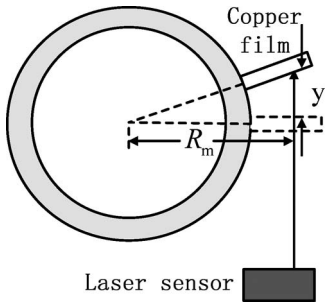

Fig. 6. Experimental setup to measure κ. The copper film is attached perpendicular to the outer surface at the tube bottom.

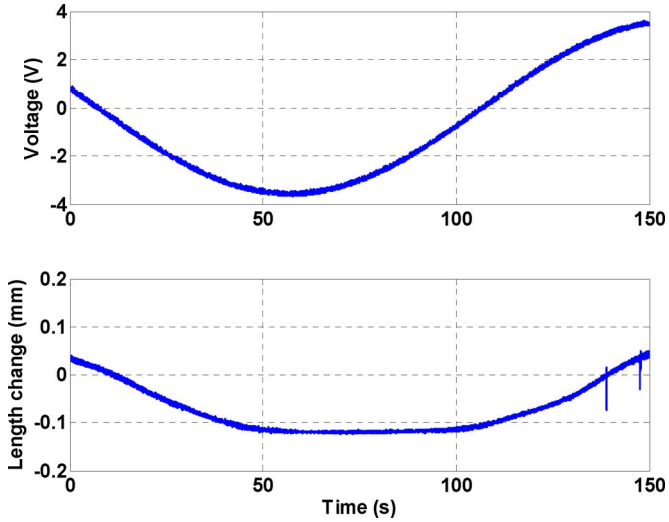

Fig. 7. Change of tube length under a 0.005-Hz sinusoidal voltage input for Sample 1.

different pitch angle (60°). All four samples had the same length (33.5 mm).

In experiments, a platinum fiber-directed PPy tube was soaked in the solution of 0.1 M Li^+TFSI^- in PC. A voltage was applied between the PPy tube and the auxiliary electrode, the latter being a stainless-steel mesh as described in Section II. The tube was fixed at the top end. To meet the quasi-static condition, a 0.005-Hz, 3.6-V sinusoidal voltage input was applied in all experiments. As discussed in Section III, three variables characterize the actuator deformation: the twist per unit length κ, the inner radius r_i, and the elongation per unit length λ_z. A laser sensor (Model OADM 20I6441/S14F from Baumer Electric, resolution $\pm 4\mu$m) was used to obtain these variables (or their equivalent) by measuring the distance to a small sticky copper film (from 3M) that was glued appropriately to the PPy tube, where the attachment method depended on the variable to be measured. For example, Fig. 6 illustrates how the twist κ was measured. The copper film was attached to the outer surface of the tube at its bottom, with the plane of the film perpendicular to the tube surface. Prior to actuation, the laser beam was set to be perpendicular to the copper film, with R_m denoting the corresponding distance between the tube center and the laser incident point on the film. In the experiments, $R_m = 4$ mm. Upon actuation, the measured displacement y of the laser incident point is related to κ via

$$y = R_m \tan(\kappa L) \tag{40}$$

where L is the length of the tube. On the other hand, the linear displacement of the tube bottom D, which is the length change of the tube, is related to λ_z via $D = (\lambda_z - 1)L$. Finally, the inner radius r_i was measured directly with a caliper.

Since the laser sensor could measure only one variable at a time, the torsional displacement y, the tube length change D, and the inner radius r_i were measured separately, and then, synchronized through the voltage input signal. Care was taken in experiments to minimize the discrepancies between the initial conditions of the actuator when measuring different variables. For a quasi-static voltage input U, we expect these variables at any time t to be functions of the instantaneous value $U(t)$. However, it was observed that sometimes the actuator output did not return to the original value when its input attained the same value. This phenomenon was likely due to the creep [35] and hysteresis behaviors of PPy actuators, and it will be a subject of future study.

Each experiment was limited to a duration of 150 or 200 s. This was primarily motivated by two considerations. First, because of the creep effect, the actuator output could undergo noticeable drift under longer experiments and thus shadow the actuation-induced effect. Second, as explained earlier, each experiment had to be repeated three times for the measurement of three output variables. Running the experiments much longer would make it difficult to ensure relatively close initial conditions for all three trials for each sample.

B. Experimental Results and Discussion

Figs. 7–9 show the experimental results on actuation-induced deformation for Sample 1. As predicted by the nonlinear elasticity theory, the actuator did demonstrate all three deformation modes: elongation, radial dilation, and torsion. From Figs. 7–9, it can be seen that both the length change and the torsional displacement correlate positively with the applied voltage, while the radius change has a reverse trend. As discussed in Section III-C, we have also solved the nonlinear elasticity-based model for the twist κ and the inner radius r_i by taking the measured elongation per unit length λ_z as given. From Figs. 8 and 9, the model is able to predict the variation of the inner radius and the torsion with respect to the voltage reasonably well.

Fig. 10 shows the measured and model-predicted torsion for Sample 2. The measured peak-to-peak torsion was about $7.4^\circ/\mathrm{m}$, and thus, smaller than what was achieved by Sample 1 ($9.2^\circ/\mathrm{m}$). From Fig. 10, the model has provided a reasonable prediction on both the magnitude and phase of the torsion,

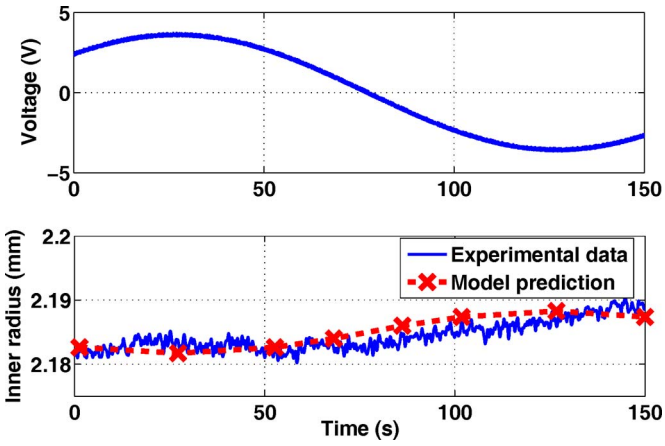

Fig. 8. Change of inner radius under a 0.005-Hz sinusoidal voltage input for Sample 1.

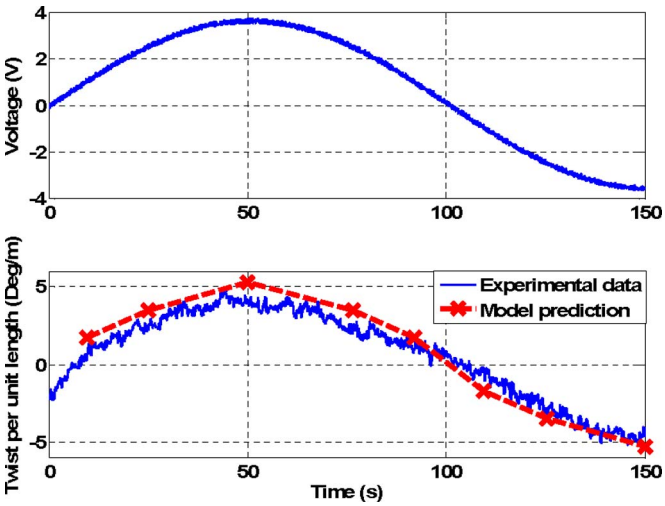

Fig. 9. Torsion κ under a 0.005-Hz sinusoidal voltage input for Sample 1.

without the need for parameter retuning. Since Sample 1 and Sample 2 differed only in inner radius, the results suggest that a larger tube radius leads to larger torsional output. We note that the measured torsion response in Fig. 10 had a trapezoidal shape, and the error between the measured and predicted torsion responses was relatively big between the extremal points. This behavior could result from imperfect actuator fabrication, or from nonideal experimental conditions, and more tests would be required to confirm or elucidate the observed phenomenon.

Fig. 11 shows the torsion of Sample 3 under the same actuation voltage, as earlier. The measured peak-to-peak torsion was about $2.1^\circ/\mathrm{m}$, and thus, much lower than that achieved by Sample 1. This implies that, for the same applied voltage, a thicker actuator generates smaller torsion. This is understandable—if we borrow the concept from linear elasticity, the torsional spring constant is bigger for a thicker tube. Fig. 12 shows the performance of torsional actuation for Sample 4. Comparing with Sample 3, Sample 4 had the same tube radius and thickness, but with a smaller pitch angle for the fiber winding. The peak-to-peak torsion reaches $4.6^\circ/\mathrm{m}$ for Sample 4, suggesting the significant influence of the pitch angle. We also note from

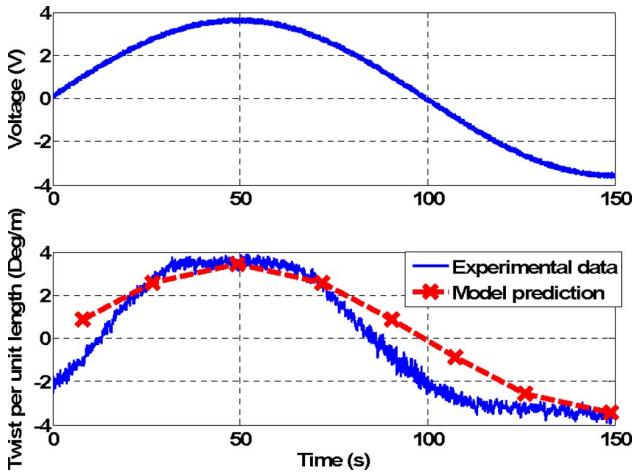

Fig. 10. Torsion κ under a 0.005-Hz sinusoidal voltage input for Sample 2. Sample 2 had the same thickness (0.381 mm) and pitch angle (80°) as Sample 1, but with smaller inner radius (1.3 mm versus 2.2 mm).

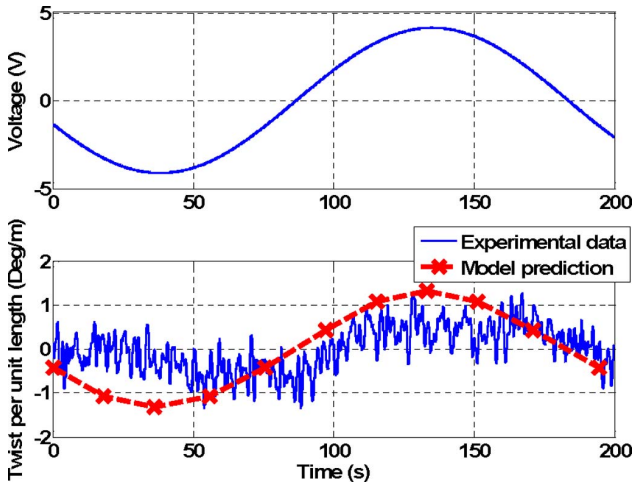

Fig. 11. Torsion κ under a 0.005-Hz sinusoidal voltage input for Sample 3. Sample 3 had the same pitch angle (80°) and inner radius (2.2 mm) as Sample 1, but with larger thickness (0.686 mm versus 0.381 mm).

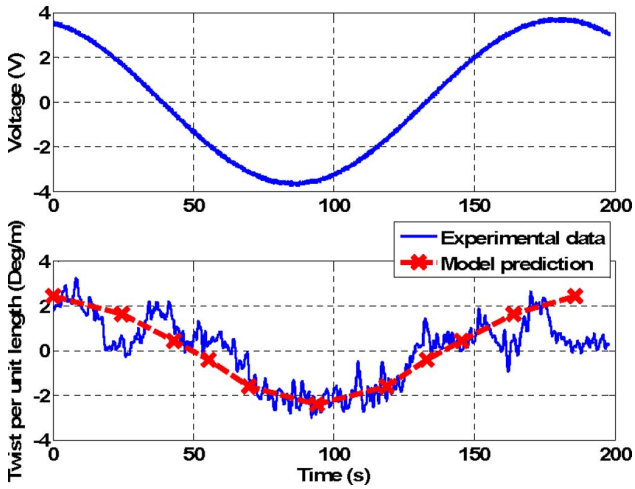

Fig. 12. Torsion κ under a 0.005-Hz sinusoidal voltage input for Sample 4. Sample 4 had the same thickness (0.686 mm) and inner radius (2.2 mm) as Sample 3, but with smaller pitch (60° versus 80°).

both Figs. 11 and 12, that a good match was achieved between experimental measurements and model-based predictions.

It is to be noted that the aforementioned results indicate that the magnitude of the torsional output κ correlates in a positive fashion with the inner radius, and correlates in a negative fashion with the thickness and pitch angle. As regards to the influence of the pitch angle, it is important to realize that both axially aligned fibers ($\beta = 0^\circ$) and purely circumferential fibers ($\beta = 90^\circ$) cannot give torsion, so that an optimal pitch angle for torsion will occur at an intermediate value.

V. Conclusion

In this paper, a novel concept for a torsional actuator has been proposed by embedding helical fibers into a conjugated-polymer tube. Actuation-induced swelling, together with fiber-introduced material anisotropy, results in torsion and other associated deformation modes. A nonlinear elasticity-based modeling framework has been presented for understanding and predicting the deformation. Experiments on four prototype samples, made of platinum fiber-directed PPy tubes, have confirmed the capability of such actuators to produce torsion and have also validated the predictive power of the nonlinear mechanics-modeling approach. In particular, we have investigated the influence of geometric parameters of the actuator (inner radius, thickness, and pitch angle) on the torsion output with both experimentation and modeling.

We note that several classes of torsional actuators have been reported in literature, which are based on electrostatic actuation [36], [37], piezoelectric materials [38], or shape memory alloy (SMA) materials [39]. While each class of actuators has its own characteristics, the fiber-directed conjugated-polymer-based torsional actuator presented in this paper has several unique advantages. It does not require high-voltage actuation as typical for electrostatic or piezoelectric actuators, and unlike SMA actuators, it generates little heat in actuation. These properties, together with the biocompatibility of the material, make the proposed actuator an ideal candidate for biomedical and biological applications. In addition, this paper supports a general principle of generating complex deformation with fiber-directed swelling, and it can have implications in developing actuators capable of other sophisticated motions using conjugated polymer or other electroactive polymers, such as ionic polymer-metal composites (IPMCs) [40], [41].

Future work will be pursued in a few directions. First, we will investigate both the nonlinear model-based geometric optimization and improvement of fabrication processes, so as to increase the torsional displacement. The torsion produced by the prototypes reported in this paper is relatively small. In addition to the fact that the geometric parameters for the samples are not optimized, we believe that the stiffness of platinum wire severely impedes the motion. Therefore, methods of embedding other types of fibers, including nonconducting ones, should be examined. Second, the discrepancies between the model predictions and the experimental measurements observed in this paper suggest that pronounced creep and hysteresis behaviors exist for the fabricated torsional actuators. It will be of interest to examine the modeling and compensation of these undesirable effects. Third, the experimental results reported in Section IV-B focused upon unconstrained torsional displacement. Alternatively, actuator devices could be deployed so as to provide a torque. We will investigate the torque performance of the torsional actuator, by developing an suitable apparatus for torque measurement and by extending the modeling analysis in this paper. Finally, device applications involving the proposed torsional actuators will be explored.

Acknowledgment

The authors would like to thank Prof. H. Demirkoparan at Carnegie Mellon University, Qatar, for helpful discussions regarding solving the nonlinear elasticity model, Prof. G. Alici from the University of Wollongong, Australia, for providing useful information on PPy fabrication, as well as the anonymous reviewers for their valuable comments that helped improve the manuscript.

References

[1] G. G. Wallace, G. M. Spinks, L. Kane-Maguire, and P. R. Teasdale, *Conductive Electroactive Polymers: Intelligent Materials Systems*, 2nd ed. Boca Raton, FL: CRC Press, 2003.

[2] E. Smela, "Conjugated polymer actuators for biomedical applications," *J. Adv. Mater.*, vol. 15, no. 6, pp. 481–494, 2003.

[3] G. Alici, G. M. Spinks, J. D. Madden, Y. Wu, and G. G. Wallace, "Response characterization of electroactive polymers as mechanical sensors," *IEEE/ASME Trans. Mechatronics*, vol. 13, no. 2, pp. 187–196, Apr. 2008.

[4] Y. Fang, X. Tan, A. Temme, and G. Alici, "Characterization and modeling of conjugated polymer sensors," in *Electroactive Polymer Actuators and Devices (EAPAD) X, Proceedings of the SPIE*, Y. Bar-Cohen, Ed., vol. 6927, 2008, pp. 692 709-1–692 709-9.

[5] R. Baughman, "Conducting polymer artificial muscles," *Synthetic Metals*, vol. 78, pp. 339–353, 1996.

[6] P. G. A. Madden, "Development and modeling of conducting polymer actuators and the fabrication of a conducting polymer based feedback loop," Ph.D dissertation, MIT, Cambridge, MA, 2003.

[7] G. Alici, P. Metz, and G. M. Spinks, "A methodology towards geometry optimization of high performance polypyrrole (PPy) actuators," *Smart Mater. Struct.*, vol. 15, pp. 243–252, 2006.

[8] Y. Fang, X. Tan, and G. Alici, "Robust adaptive control of conjugated polymer actuators," *IEEE Trans. Control Syst. Technol.*, vol. 14, no. 6, pp. 600–612, Jul. 2008.

[9] S. W. John, G. Alici, and C. D. Cook, "Validation of resonant frequency model for polypyrrole trilayer actuators," *IEEE/ASME Trans. Mechatronics*, vol. 13, no. 4, pp. 401–409, Aug. 2008.

[10] S. W. John, G. Alici, and C. D. Cook, "Inversion-based feedforward control of polypyrrole trilayer bender actuators," *IEEE/ASME Trans. Mechatronics*, vol. 15, no. 1, pp. 149–156, Feb. 2009.

[11] C. Immerstrand, K. H. Peterson, K.-E. Magnusson, E. W. H. Jager, M. Krogh, M. Skoglund, A. Selbing, and O. Inganas, "Conjugated-polymer micro- and milliactuators for biological applications," *Mater. Res. Soc. Bull.*, vol. 27, no. 6, pp. 461–464, 2002.

[12] Y. Wu, D. Zhou, G. Spinks, P. Innis, and G. Wallace, "Titan: A conducting polymer based microfluidic pump," *Smart Mater. Struct.*, vol. 14, pp. 1511–1516, 2005.

[13] Y. Fang and X. Tan, "A novel diaphragm micropump actuated by conjugated polymer petals: Fabrication, modeling, and experimental results," *Sens. Actuators A, Phys.*, vol. 158, pp. 121–131, 2010.

[14] J. Tangorra, P. Anquetil, T. Fofonoff, A. Chen, M. Del Zio, and I. Hunter, "The application of conducting polymers to a biorobotic fin propulsor," *Bioinspiration Biomimetics*, vol. 2, pp. S6–S17, 2007.

[15] S. McGovern, G. Alici, V. T. Truong, and G. Spinks, "Finding NEMO (Novel Electromaterial Muscle Oscillator): A polypyrrole powered robotic fish with real-time wireless speed and directional control," *Smart Mater. Struct.*, pp. 095 009-1–095 009-10, 2009.

[16] T. J. Pence and H. Tsai, "Swelling induced cavitation of elastic spheres," *Math. Mech. Solids*, vol. 11, pp. 527–551, 2006.
[17] J. Merodio and R. W. Ogden, "Mechanical response of fiber-reinforced incompressible non-linearly elastic solids," *Int. J. Non-Linear Mech.*, vol. 40, pp. 213–227, 2005.
[18] Z. Guo, X. Peng, and B. Moran, "Mechanical response of neo-Hookean fiber reinforced incompressible nonlinearly elastic solids," *Int. J. Solids Struct.*, vol. 44, pp. 1949–1969, 2006.
[19] H. Demirkoparan and T. J. Pence, "Torsional swelling of a hyperelastic tube with helically wound reinforcement," *J. Elasticity*, vol. 92, pp. 61–90, 2008.
[20] A. Care, L. Nefedev, B. Bonnet, B. Millet, and P. Badot, "Cell elongation and revolving movement in phaseolus vulgaris l. Twining shoots," *Plant Cell Physiol.*, vol. 39, pp. 914–921, 1998.
[21] C. Lloyd and J. Chan, "Microtubules and the shape of plants to come," *Nature Rev.: Mol. Cell Biol.*, vol. 5, pp. 13–22, 2004.
[22] R. Elbaum, S. Gorb, and P. Fratzl, "Structures in the cell wall that enable hygroscopic movement of wheat awns," *J. Struct. Biol.*, vol. 164, pp. 101–107, 2008.
[23] J. Ding, L. Liu, G. M. Spinks, D. Zhou, G. G. Wallace, and J. Gillespie, "High performance conducting polymer actuators utilising a tubular geometry and helical wire interconnects," *Synthetic Metals*, vol. 138, pp. 391–398, 2003.
[24] A. Della Santa, D. De Rossi, and A. Mazzoldi, "Characterization and modelling of a conducting polymer muscle-like linear actuator," *Smart Mater. Struct.*, vol. 6, pp. 23–34, 1997.
[25] M. Kaneko and K. Kaneto, "Electrochemornechanical deformation in polyaniline and poly(o-methoxyaniline)," *Synthetic Metals*, vol. 102, pp. 1350–1353, 1999.
[26] Y. Fang, T. Pence, and X. Tan, "Nonlinear elastic modeling of differential expansion in trilayer conjugated polymer actuators," *Smart Mater. Struct.*, vol. 17, pp. 65 020-1–65 020-10, 2008.
[27] C. Zoski Ed., *Handbook of Electrochemistry*. Amsterdam, The Netherlands: Elsevier, 2007.
[28] J. D. W. Madden, "Conducting polymer actuators," Ph.D. dissertation, MIT, Cambridge, MA, 2000.
[29] Y. Fang, X. Tan, Y. Shen, N. Xi, and G. Alici, "A scalable model for trilayer conjugated polymer actuators and its experimental validation," *Mater. Sci. Eng. C, Biomimetic Supramolecular Syst.*, vol. 28, pp. 421–428, 2008.
[30] Y. Fang, X. Tan, and G. Alici, "Redox level-dependent impedance model for conjugated polymer actuators," *Sens. Actuators B, Chem.*, vol. 132, pp. 182–190, 2008.
[31] Q. Pei and O. Inganäs, "Electrochemical applications of the bending beam method. 1. Mass transport and volume changes in polypyrrole during redox," *J. Phys. Chem.*, vol. 96, pp. 10 507–10 514, 1992.
[32] S. Therkelsen, "Constitutive modeling of active polymers," Master's thesis, MIT, Cambridge, MA, 2005.
[33] G. Qiu and T. Pence, "Remarks on the behavior of simple directionally reinforced incompressible nonlinearly elastic solids," *J. Elasticity*, vol. 49, pp. 1–30, 1997.
[34] K. Chen, L. Zhao, J. Tse, and J. Rodgers, "Elastic properties of platinum rh and rh3x compounds," *Phys. Lett. A*, vol. 331, pp. 400–403, 2004.
[35] G. Alici and N. N. Huynh, "Performance quantification of conducting polymer actuators for real applications: A microgripping system," *IEEE/ASME Trans. Mechatronics*, vol. 12, no. 1, pp. 73–84, Feb. 2007.
[36] J.-L. A. Yeh, H. Jiang, and N. C. Tien, "Integrated polysilicon and DRIE bulk silicon micromachining for an electrostatic torsional actuator," *J. Microelectromech. Syst.*, vol. 8, no. 4, pp. 456–465, 1999.
[37] J. Kim, H. Choo, L. Lin, and R. S. Muller, "Microfabricated torsional actuator using self-aligned plastic deformation," in *Proc. 12th Int. Conf. Solid-State Sens. Actuators, Transducers 2003*, Boston, MA, 2003, pp. 1015–1018.
[38] A. E. Glazounov, Q. M. Zhang, and C. Kim, "Torsional actuator and stepper motor based on piezoelectric d_{15} shear response," *J. Intell. Mater. Syst. Struct.*, vol. 11, pp. 456–468, 2000.
[39] H. Prahlad and I. Chopra, "Modeling and experimental characterization of SMA torsional actuators," *J. Intell. Mater. Syst. Struct.*, vol. 18, pp. 29–38, 2007.
[40] Z. Chen and X. Tan, "A control-oriented and physics-based model for ionic polymer-metal composte actuators," *IEEE/ASME Trans. Mechatronics*, vol. 13, no. 5, pp. 519–529, Jul. 2008.
[41] Z. Chen and X. Tan, "Monolithic fabrication of ionic polymer-metal composite actuators capable of complex deformation," *Sens. Actuators A, Phys.*, vol. 157, pp. 246–257, 2010.

Yang Fang (S'06–M'08) received the B.S. degree in automatic control from the University of Science and Technology of China, Hefei, China, in 2003, the M.S. degree in manufacturing systems and technology from Nanyang Technological University, Singapore, in 2005, and the Ph.D. degree in electrical engineering from Michigan State University, East Lansing, in 2009. His Ph.D. dissertation research was focused on modeling, control, and applications of conjugated polymer actuators and sensors.

Since 2009, he has been with the Engine, Emissions and Vehicle Research Division, Southwest Research Institute, Ann Arbor, MI, where he has been involved in developing novel control strategies for hybrid vehicles and applying smart material sensors to increase fuel efficiency. He has authored or coauthored more than ten technical peer-reviewed papers.

Dr. Fang was the recipient, along with Dr. X. Tan, of the 2008 Best Mechatronics Paper Award from the ASME Dynamic Systems and Control Division.

Thomas J. Pence received the B.S. degree in engineering mechanics from Michigan State University, East Lansing, in 1979, and the M.S. and Ph.D. degrees in applied mechanics from California Institute of Technology, Pasadena, CA, in 1980 and 1983, respectively.

He was a Summer Intern at Argonne National Laboratory. He was a Visiting Summer Engineer at Exxon Production Research, Houston, TX. During 1983–1984 and 1985–1986, he was a Van Vleck Assistant Professor of Applied Mathematics at the University of Wisconsin (U.W.), Madison and at the U.W. Mathematics Research Center. During 1984–1985, he was a North Atlantic Treaty Organization (NATO) Postdoctoral Researcher in the Department of Numerical Analysis, University of Paris–Orsay. Since 1986, he has been at Michigan State University, where he is currently a Professor of mechanical engineering. During this time, he has held sabbatical appointments at the University of Rome (Department of Structural and Geotechnical Engineering, Roma 1 (La Sapienza) and Department of Civil Engineering, Roma 3) and in the Department of Mathematics, University of Glasgow, Glasgow, U.K. His research interests include the mechanical behavior of highly deformable solids, with modeling application to polymers, elastomers, phase transformations (including shape memory materials), gels, and soft tissue. He is currently on the Editorial Boards of the *Journal of Elasticity* and *Continuum Mechanics and Thermodynamics.*

Xiaobo Tan (S'97–M'02) received the B.Eng. and M.Eng. degrees in automatic control from Tsinghua University, Beijing, China, in 1995 and 1998, respectively, and the Ph.D. degree in electrical and computer engineering from the University of Maryland, College Park, in 2002.

From September 2002 to July 2004, he was a Research Associate at the Institute for Systems Research, University of Maryland. Since August 2004, he has been an Assistant Professor in the Department of Electrical and Computer Engineering, Michigan State University (MSU), East Lansing, where he is also the Director of the Smart Microsystems Laboratory. He is keen to integrate his research with educational and outreach activities, and leads a National Science Foundation (NSF)-funded Research Experiences for Teachers Site on Bio-Inspired Technology and Systems at MSU. His current research interests include electroactive polymer sensors and actuators, biomimetic robotic fish, mobile sensing in aquatic environments, modeling and control of smart materials, and collaborative control of autonomous systems.

Dr. Tan has served as an Associate Editor of *Automatica* since 2008, and has served on the Conference Editorial Board of the IEEE Control Systems Society since 2007. He was a Guest Editor of *IEEE Control Systems Magazine* for its February 2009 issue's Special Section on Modeling and Control of Hysteresis. He was the recipient of an NSF Faculty Early Career Development Award in 2006, the 2008 ASME Dynamic Systems and Control Division Best Mechatronics Paper Award (with Y. Fang) in 2009, and the Teacher-Scholar Award from MSU in 2010.